Journal of Hydrology 501 (2013) 163–174

Contents lists available at ScienceDirect

Journal of Hydrology

journal homepage: www.elsevier.com/locate/jhydrol

Hydrogeochemical niches associated with hyporheic exchange beneath an acid mine drainage-contaminated stream

Lance N. Larson [a], Michael Fitzgerald [b,c], Kamini Singha [d], Michael N. Gooseff [e], Jennifer L. Macalady [b], William Burgos [a,*]

[a] Department of Civil and Environmental Engineering, The Pennsylvania State University, University Park, PA 16802, USA
[b] Department of Geosciences, The Pennsylvania State University, University Park, PA 16802, USA
[c] Aquatics Team, National Ecological Observatory Network, Inc. (NEON, Inc.), Boulder, CO 80301, USA[1]
[d] Hydrologic Science and Engineering Program, Colorado School of Mines, Golden, CO 80401, USA[1]
[e] Department of Civil & Environmental Engineering, Colorado State University, Fort Collins, CO 80523, USA[1]

ARTICLE INFO

Article history:
Received 5 January 2013
Received in revised form 3 August 2013
Accepted 5 August 2013
Available online 14 August 2013
This manuscript was handled by Peter K. Kitanidis, Editor-in-Chief, with the assistance of Xunhong Chen, Associate Editor

Keywords:
Iron cycling
Hyporheic exchange
Coal mine drainage
In situ pore-water

SUMMARY

Biological low-pH Fe(II)-oxidation creates terraced iron formations (TIFs) that remove Fe(III) from solution. TIFs can be used for remediation of acid mine drainage (AMD), however, as sediment depth increases, Fe(III)-reduction in anoxic subsurface areas may compromise treatment effectiveness. In this study we used near-surface electrical resistivity imaging (ERI) and *in situ* pore-water samplers to spatially resolve bulk conductivity changes within a TIF formed in a stream emanating from a large abandoned deep clay mine in Cambria County, Pennsylvania, USA. Because of the high fluid electrical conductivity of the emergent AMD (1860 μS), fresh water (42 μS) was added as a dilution tracer to visualize the spatial and temporal extent of hyporheic exchange and to characterize subsurface flow paths. Distinct hydrogeochemical niches were identified in the shallow subsurface beneath the stream by overlaying relative groundwater velocities (derived from ERI) with pore-water chemistry profiles. Niches were classified based on relatively "fast" versus "slow" rates of hyporheic exchange and oxic versus anoxic conditions. Pore-water concentrations and speciation of iron, pH, and redox potential differed between subsurface flow regimes. The greatest extent of hyporheic exchange was beneath the center of the stream, where a shallower (<10 cm) Fe(II)-oxidizing zone was observed. Meanwhile, less hyporheic exchange was observed near the channel banks, concurrent with a more pronounced, deeper (>70 cm) Fe(II)-oxidizing zone. At these locations, relatively slower groundwater exchange may promote biotic Fe(II)-oxidation and improve the long-term stability of Fe sequestered in TIFs.

1. Introduction

Environmental impacts associated with active and historic coal mining activities impair or threaten ecosystems throughout much of the Appalachian region of the United States. The Appalachian coal fields extend over 1600 km in length from Alabama to Pennsylvania; however, a disproportionate number of mine-impacted streams are found in Pennsylvania because of the regional coal geology (PA DEP, 1998). Ecological impairment to downstream water bodies arise as sulfide-bearing coal seams and surrounding strata are subject to chemical and physical weathering processes that generate acidity, frequently referred to as acid mine drainage (AMD) or, more specifically, coal mine drainage (CMD). CMD is characterized by elevated concentrations of dissolved metals (primarily iron, aluminum and manganese) and sulfate, and high fluid electrical conductivity (Kirby and Cravotta, 2005; Cravotta, 2008). Depending on site geology and hydrogeology, the pH and acidity of CMD can vary from low-pH and net-acid to circumneutral-pH and net-alkaline.

Our research focuses on systems where anoxic, low-pH, Fe(II)-rich AMD emerges from artesian springs, enters a stream, and immediately begins to react with the atmosphere and stream water. In these hydrogeochemical settings, biological low-pH Fe(II) oxidation leads to the precipitation of Fe(III) in the form of ferric sulfate-(hydr)oxide minerals such as schwertmannite [$Fe_8O_8(OH)_6(SO_4)$] (Bigham et al., 1996) or ferric oxyhydroxides such as ferrihydrite. Biological low-pH Fe(II) oxidation, therefore,

* Corresponding author. Address: Department of Civil and Environmental Engineering, The Pennsylvania State University, 212 Sackett Building, University Park, PA 16802, USA. Tel.: +1 814 863 0578; fax: +1 814 863 7304.
E-mail address: wdb3@psu.edu (W. Burgos).
[1] Current address.

0022-1694/$ - see front matter © 2013 Elsevier B.V. All rights reserved.
http://dx.doi.org/10.1016/j.jhydrol.2013.08.007

is an attractive option for AMD remediation because it can remove substantial amounts of Fe(III) before conventional neutralization processes. For example, limestone beds are common in passive treatment systems; however armoring of limestone and/or clogging of the limestone beds due to precipitation of Fe(III) minerals limits performance, but can be minimized by first removing Fe(III) via low-pH Fe(II) oxidation. Furthermore, the process decreases pH, which can promote alkalinity generation from limestone.

In natural or engineered settings, biologically mediated low-pH Fe(II) oxidation will create terraced iron formations (TIFs). The morphology of these TIFs is dependent on site specific hydrodynamic conditions (Veysey Ii and Goldenfeld, 2008), water chemistry, and kinetics of Fe(II) oxidation and Fe(III) precipitation. Under certain conditions TIF sediment depth can become substantial. For example, Fe-rich sediments >1 m in depth have been reported for TIFs formed from CMD in Appalachia (DeSa et al., 2010) and AMD in the Iberian Pyrite Belt (Sánchez España et al., 2007). For TIFs to remain as part of an AMD treatment system, the immobilization of Fe (via oxidative precipitation at the surface) must exceed any possible remobilization in the subsurface (via reductive dissolution). Previous studies have shown that hydrodynamic conditions (velocity and shear) in surface streams control biofilm architecture (Bottacin-Busolin et al., 2009) and microbial community composition (Macalady et al., 2008). Geochemical conditions also exert an effect on microbial community composition, especially in extreme low-pH environments (Baker and Banfield, 2003). However, hydrodynamic or geochemical conditions alone often cannot fully explain microbial diversity (Flores et al., 2012). Hydrogeochemical niches can be identified by overlaying hydrodynamic and geochemical conditions, and may improve our ability to understand and predict microbial diversity. These data are relatively straightforward to obtain in surface streams but are far more difficult to obtain in the subsurface.

In-steam measurements, or measurements from limited available wells, make characterization of groundwater-surface water exchange processes difficult. Geophysical tools are starting to become commonly used in these systems; in particular, electrical resistivity is now frequently used to monitor exchange and understand flow paths (Ward et al., 2010; Cardenas and Markowski, 2010; Coscia et al., 2011; Toran et al., 2012; Doro et al., 2013). Electrical methods have long been used to image groundwater contamination associated with AMD (Merkel, 1972; Ebraheem et al., 1990; Rucker et al., 2009); however, application of these techniques to quantify hyporheic exchange in an AMD-impacted river, to the best of our knowledge, has not yet been considered. Here, we capitalize on this previous work in a new setting.

The objectives of the current study were to (1) resolve the spatial extent of oxic and anoxic conditions within a TIF, (2) to characterize the subsurface geochemistry in these zones, and (3) identify hydrogeochemical niches in the shallow subsurface. Geophysical techniques such as near-surface electrical resistivity imaging (ERI) used with a conductive tracer can visualize hyporheic exchange beneath a stream (e.g., Nyquist et al., 2008; Ward et al., 2010). In the current study, we used low conductivity water as the tracer because of the intrinsically high conductivity of the AMD-impacted stream. ERI methods coupled with a constant-rate, long-term tracer addition provided a 2-dimensional view of subsurface hydrodynamic conditions beneath the stream and the spatial and temporal extent of hyporheic exchange. Subsurface pore-water samplers were then deployed along electrode transects to measure geochemistry in areas of contrasting extent of hyporheic exchange. Combined, these approaches identified a variety of hydrogeochemical niches beneath the AMD-impacted stream.

2. Methods and materials

2.1. Site description

The AMD field site was located near Brubaker Run (BR) (40°37′1.42″N; 78°28′35.76″W), a small tributary of Clearfield Creek (Fig. 1); located approximately 3.2 km northwest of Altoona, PA and 2 km east of Dean, PA. The Dean Clay Mine was a 1,011,800 m^2 underground kaolinite mine that flooded after being abandoned (ca. 1950). The Dean Clay Mine now discharges AMD to Brubaker Run as a large artesian spring that was located above a former air shaft in the collapsed entry to the mine. Water flows downhill from the artesian spring across a large TIF (6000 m^2) in a highly uncontrolled, multi-directional manner, except for one large channel that was the former adit into the mine. This large channel was used for all tracer studies because of its well-constrained, uni-directional flow characteristics (Figs. 1 and 2). A second artesian spring (referred to as BR80) is located along the left-bank of this channel. All left and right-bank designations refer to a downstream orientation. The water chemistry of BR80 and the uphill artesian spring are essentially identical and BR80 is thought to emerge from the "toe" of the mine pool (versus up through the former air shaft). A large fraction of the water from the uphill spring is captured by the adit channel. The top of the uni-directional portion of this channel is approximately 20 m from the center of the uphill spring (and approximately 5 m lower in elevation). The uni-directional portion of the channel then runs for 60 m before dispersing in a multi-directional manner across a lower series of iron terraces.

Because of the high flow and high conductivity of the Dean Clay Mine discharge, a "dilution tracer" was selected containing low conductivity water collected from an adjacent headwater creek (see Table 1). Laurel Run is located near Dysart, PA, approximately 4.8 km from Brubaker Run and was never impacted by coal-mining activities. A water-hauling company was contracted to collect water from Laurel Run and deliver it via a 3000-gallon water truck parked at the test site. A coarse screen was placed on the hose during collection from Laurel Run, and the water was then pumped through 0.5 mm filter bags when fillingthe parked water truck. Water was pumped from the parked tanker through a Neptune flowmeter that was continuously monitored and maintained at 6.3–6.4 L/s for the complete 10 h tracer addition period. With no tracer addition, we estimated that approximately 3.5 L/s was entering the channel just upstream of the tracer addition zone (0 m datum), and we measured a flow of 15.8 L/s at the end of the uni-directional portion of the channel (60 m downstream). Water was pumped approximately 90 m (~10 m elevation gain) from the truck to the injection zone (BR100). The tracer addition zone was located essentially at the start of the uni-directional portion of the channel and is referred to as the 0 m datum for stream locations in this study. The injection zone consisted of a 55-gallon plastic drum equipped with a 3-in. diameter stand pipe positioned to deliver water to the bottom of the drum. Water then overfilled the drum, ran onto plywood placed beneath the drum and then into the channel (Fig. 2A). Wading surveys to measure stream flow, using a Marsh-McBirney velocimeter and wading rod, were conducted 60 m below the injection zone before and during tracer injection to evaluate how much of the tracer exited the uni-directional portion of the channel.

2.2. Electrical resistivity imaging

ERI data were collected on a network of electrodes installed in three transects oriented laterally across the stream channel using a 10-channel Syscal Pro Resistivity Meter (IRIS Instruments,

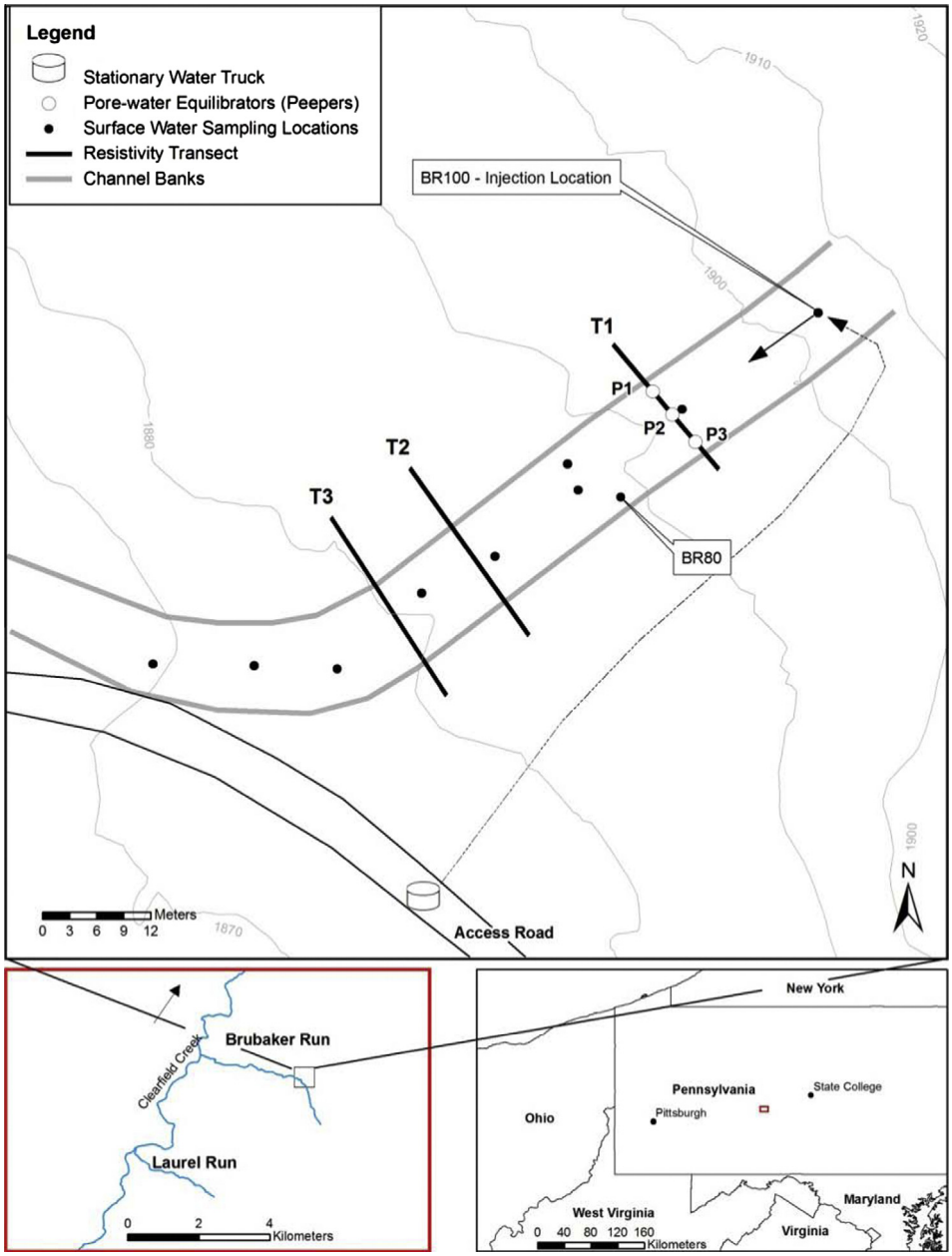

Fig. 1. Location and layout of experimental setup at Brubaker Run, near Dean, PA. Laurel Run was used for the fresh water dilution tracer. Acid mine drainage (AMD) from a large, underground clay mine emerges uphill of BR100 and flows down a channel formed from the former adit into the mine. An artesian spring at BR80 serves as a secondary source of AMD. Electrode transects for electrical resistivity imaging (ERI) were installed perpendicular to the AMD channel at T1, T2 and T3. Subsurface pore-water samplers were installed at T1 along the center of the channel. The fresh water tracer was pumped from a water truck parked on the access road to the injection location at BR100.

Orleans, France). Transects 1, 2 and 3 (T1, T2 and T3) were 20, 46, and 58 m, respectively, from the injection zone (Fig. 2B). BR80 was 30 m from the injection zone. Electrode spacing within each transect was approximately 1.0 m between electrodes in the transect center and increased to 1.5 m towards the end of each transect. Electrode positioning was selected to yield high-resolution measurements across the stream channel where change was anticipated to be greatest while also collecting measurements beyond the channel banks.

Electrodes were manufactured from ½-in. diameter schedule-40 PVC pipes approximately 0.75 m in length. Conductive foil tape was wrapped around the pipe about 10 cm from the bottom to create the electrode surface. An 18-gauge stranded wire connected the foil tape (contact surface below ground) to the trunk line of wires (solid strand 18-gauge), which connected to the ER switch box. Contact resistance of the electrodes was checked prior to the injection and ranged from 0.1 to 4.0 kOhms. The design of these foil-wrapped PVC pipes allowed the electrodes to be positioned in the subsurface without providing a direct conduit to the surface (e.g., via steel or copper pipe electrode).

A mixed dipole–dipole array with 323 measurements was used for data collection and the same sequence was utilized for all transects. The sequence was designed to maximize coverage in the stream center while minimizing the number of electrical injections to reduce temporal smearing during the test. Data collection took approximately 12 min per transect. All data were collected along individual transects; between-transect data were not collected in the interest of time.

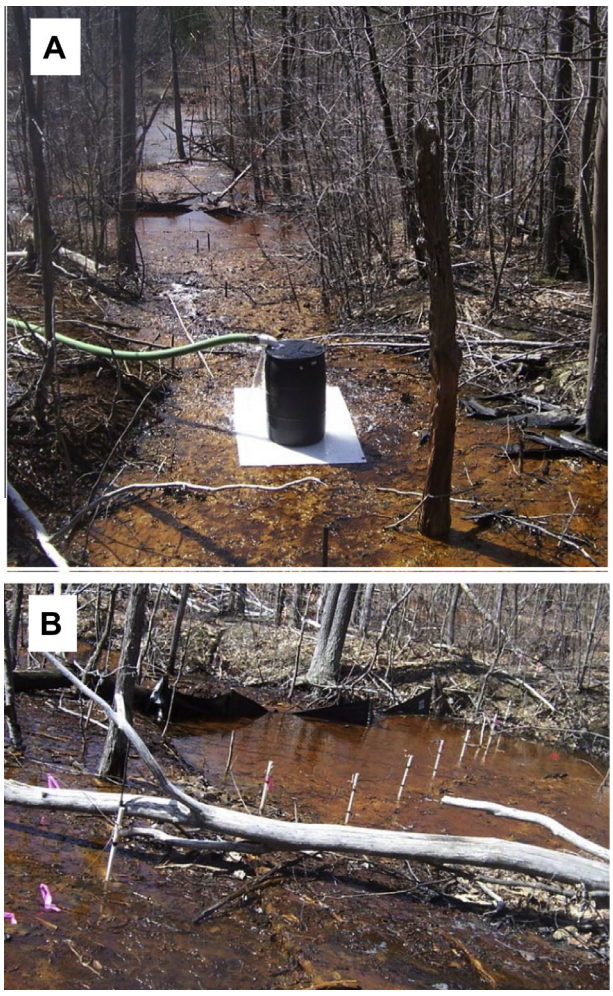

Fig. 2. Field photographs of the Brubaker Run site. (A) Downhill view of the tracer injection zone and the top of the channel (orientation for assignment of L and R bank locations). Fresh water was pumped from a truck and overfilled the barrel before flowing down the channel. (B) Electrode Transect 1 (T1) located 20 m downstream of injection zone. Twelve electrodes (placed 25 cm into the ground) were spaced 1.0–1.5 m apart and data were collected every 30–45 min during the 10 h constant-rate injection test.

Background resistivity measurements were collected across each transect three times before tracer addition, from 17:00 March 21 to 07:00 March 22, 2011. Background resistivity values for each transect were averaged from these three datasets and then used as the initial conditions to calculate relative changes in resistivity in the ERI tomograms. Resistivity measurements for T1, T2, and T3 were cycled approximately every 38 min over the entire sampling period. The tracer addition began at 08:00 and ended at 18:00 March 22, 2011. To monitor the storage and flushing of the tracer, ERI data collection continued for 60 min after the tracer addition ceased. Data quality was monitored during the tests and error was estimated using data stacking where a minimum of two measurements were collected, averaged, and standard deviation calculated on the set. Due to time constraints, reciprocal measurements were not collected. Mean stacking errors (coefficients of variation) for any transect never exceeded 0.1%, and were generally between 0.05% and 0.07%.

2.3. Surface water sampling

Before, during, and after tracer addition a series of in-stream locations were used to measure electrical conductivity of the surface water using an YSI Environmental EC 300 conductivity electrode (YSI, Yellow Springs, OH). In-stream conductivity measurements were made primarily along the center of the channel, typically in shallow pools where it was easy to fully immerse the probe.

Before and during the tracer experiment a series of in-stream locations were used to measure surface water chemistry up to 130 m downstream of the injection zone (including a section below the uni-directional portion of the channel). Portable field meters were used to measure pH and temperature [Beckman BKA57201], and oxidation–reduction potential (ORP) [Beckman A57197]. Water samples were collected at each location, filtered (0.2 μm), chemically preserved (analyte-dependent), and stored on ice before analysis. These measurements were made at 07:00 March 22, 2011 (before injection) and 14:00 March 22, 2011 (during injection), and a similar set of in-stream samples were collected on 12:00 July 28, 2011 when subsurface pore-water samplers were removed from the site (described below).

2.4. Subsurface pore-water sampling

Subsurface chemistry profiles were measured using *in situ* pore-water equilibration samplers (referred to as "peepers"), previously designed, built, and used by Johnston et al. (2009). Three peepers were installed across T1 (Fig. 1), one near each channel bank and one in the center of the channel. Peepers were constructed from solid 3-in. diameter high density polyethylene and had a series of 2.6 cm diameter holes cross-drilled horizontally through the peeper frame at a vertical spacing interval of 5 cm. Each peeper was 1.52 m in length and held 25 sample vials. Sample vials were 26 mm dia, 25 mL polypropylene vials that were fitted with a 47 mm dia., 0.2 μm Tuffryn® Membrane Filter (Pall Life Sciences, Ann Arbor, Michigan) and sealed with a 26 mm threaded "annulus" cap. The cap left a 12 mm dia membrane circle exposed to adjacent pore-water. Sample vials were filled with 100% N_2-purged, distilled and de-ionized (d–d) water, capped, and stored overnight in a d–d water bath continuously flushed with N_2 prior to field deployment. A portable bottle of nitrogen gas was used to flush the water bath as sample vials were transported to the field site (<1.5 h). Pre-labeled sample vials were quickly loaded into the peeper frame to minimize atmospheric O_2 exposure. We estimate that sample

Table 1
Geochemical characteristics of emergent acid mine drainage (AMD) into Brubaker Run and low conductivity tracer collected from Laurel Run.

	pH	ORP (mV)	Conductivity (μS/cm)	Temp (°C)	Discharge[a] (L/s)	Al	Ca	Co	Cu	Fe	K	Mg	Mn	Na	Ni	S	Zn
AMD Source (BR 80)	3.34	404	1863	11.0	7.8 ± 2.8	0.47	3.1	0.01	BDL	1.5	0.14	4.4	0.53	0.48	0.015	10.9	0.026
Injection Water (Laurel Run)	6.21	405	42	7.6	6.3 ± 0.3	0.004	0.052	BDL	BDL	BDL	0.02	0.03	0.002	0.05	BDL	0.07	BDL

BDL – Below Detection Limit.
All concentrations are mM.
% error weir/wading survey: 3.2–10.8%
[a] Estimated with weir calculations and wading surveys.

vials were exposed to the atmosphere for no more than 15 min before each peeper was pushed into the ground. Peepers were manually pushed into the streambed sediments to their complete depth, assisted in some cases with a post-hole driver, or embedded incompletely to the point of first refusal. Care was taken not to push the peepers too hard and possibly shear off the membranes in the sample vial caps. The peepers were installed on July 1, 2011 and removed on July 28, 2011. This 27 d equilibration period was similar to a recommended equilibration time of 30 d (Hesslein, 1976; Johnston et al., 2009).

The peepers were manually removed from the sediments and all sample vials were quickly transferred to portable glove bags (Aldrich® Atmosbag) that were constantly flushed with helium gas. The integrity of each sample vial membrane/cap was checked based on the absence of turbidity or the absence of any gas bubbles in the vials. Vials that failed this quality control check were not analyzed. The He-purged portable glove bags were sealed after all sample vials were removed from the peepers, transported back to our laboratory, and then opened inside an anoxic chamber (Coy, Grass Lakes, MI) supplied with a 95:5% N_2:H_2 gas mix. Samples were stored in the anoxic chamber until analysis (<1 d).

2.5. Analytical methods

Peeper vials were opened inside the anoxic chamber and split into multiple plastic sample bottles for various analyses. The remainder of sample was analyzed directly for pH (Mettler Toledo–InLab* Mini pH Electrode), ORP (Mettler Toledo–InLab*Redox Mini Electrode), and conductivity [Thermo Orion 105A+]. All ORP values are reported relative to an Ag/AgCl reference electrode. Samples were preserved with HCl and dissolved Fe(II) was measured using the ferrozine assay (Stookey, 1970). Samples for total dissolved iron were first reacted with 0.5 M hydroxylamine–HCl and then measured by ferrozine. Dissolved Fe(III) was operationally defined as the difference between total dissolved iron and dissolved Fe(II).

2.6. Electrical resistivity modeling methods

Electrical resistivity data inversion was completed using the code R2 (v2.6, Generalized 2-D Inversion of Resistivity Data, available online at: http://www.es.lancs.ac.uk/people/amb/Freeware/freeware.htm). The algorithm, which is based on Occam's inversion, is described in Binley and Kemna (2005). Data collected during and after tracer addition were inverted using the background resistivity distribution as a starting model. The background resistivity image was differenced from each of the images collected during and after the tracer study by calculating the percent change in resistivity ($\Delta\rho$) for each pixel. The percent difference tomograms show the low conductivity-labeled surface water mixing into the subsurface.

3. Results

3.1. In-channel conductivity

The conductivity in the surface water at each transect responded quickly to the beginning and end of tracer addition (Fig. 3). At T1, 20 m downstream of the tracer injection zone and upstream of BR80, the pre-test conductivity was 1800 μS and decreased to 861 μS within 40 min after tracer addition began. The conductivity at T1 continued its rapid decrease (to 597 μS after 90 min), then remained relatively constant for the next several hours and finally increased to ca. 1000 μS for the final 3 h of the tracer addition period. Conductivity measurements at T1 displayed greater variability as

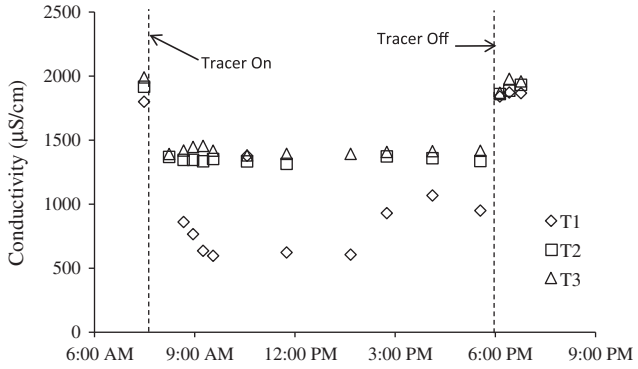

Fig. 3. In-stream conductivity measurements before, during, and after tracer addition. A 10 h constant rate addition of fresh water tracer began at 8:00 AM and ended at 6:00 PM (denoted by vertical dashed lines). Transect 1 (T1) was 20 m downstream of the tracer injection zone and upstream of the artesian spring BR80. Transect 2 (T2) was 46 m downstream of the tracer injection zone and 7 m downstream of BR80. Transect 3 (T3) was 58 m downstream of the tracer injection zone.

compared to the near-constant conductivity measurements at T2 and T3 during tracer addition. In-stream mixing of the tracer with the channel water may have been more homogeneous at T2 and T3 when compared to = T1, causing these differences. After tracer addition ceased, the conductivity at T1 returned to pre-test levels (1841 μS) by the first post-test measurement.

At T2, 46 m downstream of the tracer injection zone and 16 m downstream of BR80, the pre-test conductivity dropped from 1917 μS to 1369 μS within 14 min after tracer addition began and remained relatively constant for the 10 h duration of the test. Similar temporal patterns were observed at T3. The smaller extent of decrease in conductivity at T2 and T3, as compared to T1, was caused by the addition of high conductivity water from the artesian spring located at BR80.

Wading surveys conducted just below T3 before and during tracer addition confirmed that the entire added tracer flow was exiting the uni-directional channel during tracer addition. The measured flow at T3 before tracer addition was 15.8 L/s and then increased to 21.7 L/s after the start of tracer addition. This increase in flow nearly equaled the tracer flow (6.3 L/s), a quantity that was continuously measured during the test. Therefore, using an analogous flow balance at T1 and using conductivity as a conservative tracer, we used a flow-weighted summation to calculate the flow rate of water entering the uni-directional channel just upstream of BR100 (presented in Supplementary data). Based on this conductivity summation, we estimate approximately 3.5 ± 1.7 L/s was entering the channel upstream during tracer addition. In a similar manner, using conductivity values measured at BR80 and downstream of T3, we used a flow-weighted summation to calculate that approximately 12.5 ± 1.8 L/s of AMD entered the channel at BR80. Because of its artesian nature and physical location, the flow rate of BR80 was otherwise virtually impossible to measure directly.

3.2. Surface water chemistry

The geochemistry of the water at the top of the channel varied considerably compared to the headwater at the uphill spring. The uphill spring was anoxic, with Fe(II) as the predominant Fe valence state. As this water became aerated, biological low-pH Fe(II) oxidation occurred and Fe(III) produced from this process precipitated out of solution as schwertmannite and ferrihydrite (Burgos et al., 2012). Fe(III) precipitation consumed alkalinity and decreased the pH. Thus, the typical geochemical gradients downstream of

an acidic, anoxic, Fe(II)-rich spring will be for dissolved oxygen and ORP to increase; and for dissolved Fe(II), dissolved total Fe, and pH to decrease.

This generalization becomes more complicated in the current study because of the addition of the dilution tracer and the addition of BR80, a large anoxic, artesian source. The addition of BR80 into the channel effectively "reset" the geochemical gradients that had begun to establish in between the uphill spring and BR80. This was most evident with concentrations of dissolved Fe(II) (Fig. 4C). Dissolved Fe(II) concentrations increased in the channel due to the artesian spring at BR80 but immediately began to decease because of biological Fe(II) oxidation and Fe(III) precipitation in the channel. The addition of 6.3 L/s of the low conductivity tracer (42 μS, pH 6.2, 8.0 mg/L O_2, 450 mV ORP, <0.1 mg/L Fe) to the channel acutely modified the water chemistry and geochemical gradients in the channel (Fig. 4). While the tracer had a relatively high pH, this water had very little alkalinity such that the pH of the AMD in the channel during the test increased only by ca. 0.1 unit (uniformly along the whole channel length) during tracer addition (Fig. 4A). The ORP values measured during tracer addition were quite variable. In waters with high dissolved concentrations of Fe(II) and Fe(III), both Fe(II/III) and dissolved oxygen contribute to poise ORP. During tracer addition, ORP measurements were likely confounded by the blending of the tracer and surface water. As discussed above, the conductivity of the water decreased immediately downstream of the tracer injection zone, and then increased after the addition of BR80 (Fig. 3). Iron concentrations in the channel decreased during tracer addition, however, this was likely caused by dilution effects rather than changes in Fe(II) oxidation kinetics as Fe speciation (i.e., $[Fe(II)]/[Fe]_{TOT}$) remained essentially unchanged during the test.

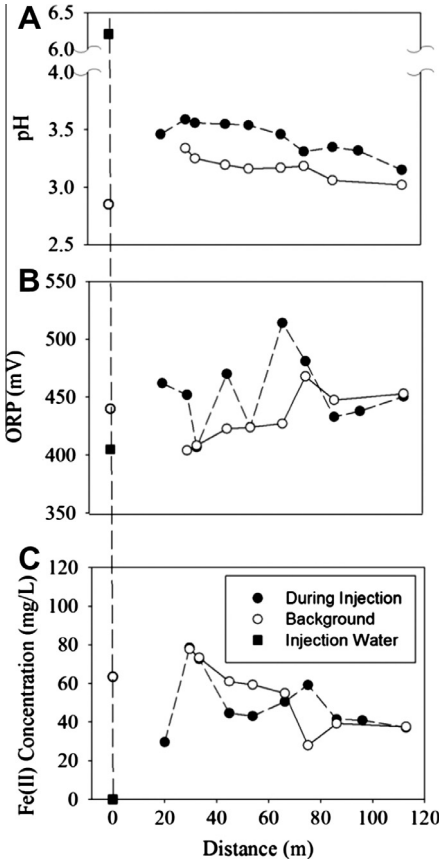

Fig. 4. Surface water geochemistry displayed as a function of distance from the tracer injection zone (0 m datum denoted with dashed vertical line). Open circles (○) are background measurements collected 1 h prior to tracer injection; closed circles (●) are measurements collected 5 h into the tracer experiment; and closed squares (■) are measurements of the tracer. The artesian spring at BR80 entered the channel at 30 m.

3.3. Electrical resistivity imaging

Time-lapse ERI results for each transect are presented in Fig. 5. Background resistivity values ranged from 10^{-1} to 10^{3} ohm-m across the three transects with lower values located within the channel. The spatial resolution of the ERI measurements cannot be quantified exactly, as it is dependent on the electrical conductivity of the subsurface and the geometry of electrodes used. Across all three transects, sensitivity values were greatest within 0–1.0 m below ground surface (b.g.s.) and decreased with depth, indicating greater reliability of imaging near the surface sediments. That is, the "trustworthiness" of data decreases with decreasing sensitivity. At T1, and T3 to a lesser degree, the sensitivity across the entire transect was uniform both laterally and vertically. At T2, low sensitivity values towards the left bank suggest a strong influence from the artesian source BR80 on resistivity measurements. From all of the ERI tomograms, the largest relative change of resistivity as compared to baseline (i.e., $\Delta\rho$) was 4.0%. While the range of relative $\Delta\rho$ was relatively small (0.23–4.0%) in this study, mean stacking errors for any transect never exceed 0.1%. The top-most row of pixels represents the net resistivity of the stream water and stream sediments within those domains.

The ERI tomograms reveal that hyporheic exchange is occurring along this stream reach. While hyporheic exchange involves the mixing of stream water and shallow groundwater, it is unique because the stream water that enters the subsurface (i.e., the hyporheic zone) eventually re-enters the stream at some point downstream (Gooseff, 2010). We operationally defined the extent of hyporheic exchange based on the penetration of the surface water tracer into the subsurface leading to measurable changes in apparent resistivity (Fig. 5). This system displays hyporheic exchange because the tracer added above T1 (Fig. 1) mixes into the subsurface beneath T1 and T2 and then re-enters the stream by T3. Detailed discussions of these transects are provided below.

The ERI tomograms displayed different characteristics at each transect. Across T1 (Fig. 5A), the tracer first arrived along the center of the channel. For T1 the largest $\Delta\rho$ value was 2.3%. As tracer addition continued, the tracer penetrated deeper into the subsurface and wider toward the stream banks. The radial expansion of tracer infiltration indicated the combination of advective and diffusive transport mechanisms within the hyporheic zone in this channel reach. The rapid infiltration of tracer indicated good connectivity between the surface water and shallow groundwater. After tracer addition ceased, the dilution tracer remained in the shallow groundwater for up to 0.5 h.

ERI tomograms for T2 (Fig. 5B) were more complicated as compared to T1, likely due to the addition of BR80 into the channel (16 m upstream of T2). For T2 the largest $\Delta\rho$ value was 4.0%. As with T1, the area of tracer infiltration expanded radially deeper into the ground and towards the stream bank. However, there were at least three important differences between the ERI tomograms collected at T1 as compared to T2. First, the expansion of the tracer signal beneath the center of the channel at T2 was non-uniform with abrupt differences in resistivity between adjacent pixels. Second, a strong transient tracer signal was observed several meters to the left of the left bank of the channel at T2. After 2.5 h of tracer addition, $\Delta\rho$ increased up to 2.5% in this region outside of the channel. After 5.5 h, the $\Delta\rho$ in this region had relaxed back to baseline levels. This suggests that the transient storage beneath the left bank endorsed preferential flow paths. Third, a large "dark void" was observed beneath the left bank of the channel where the

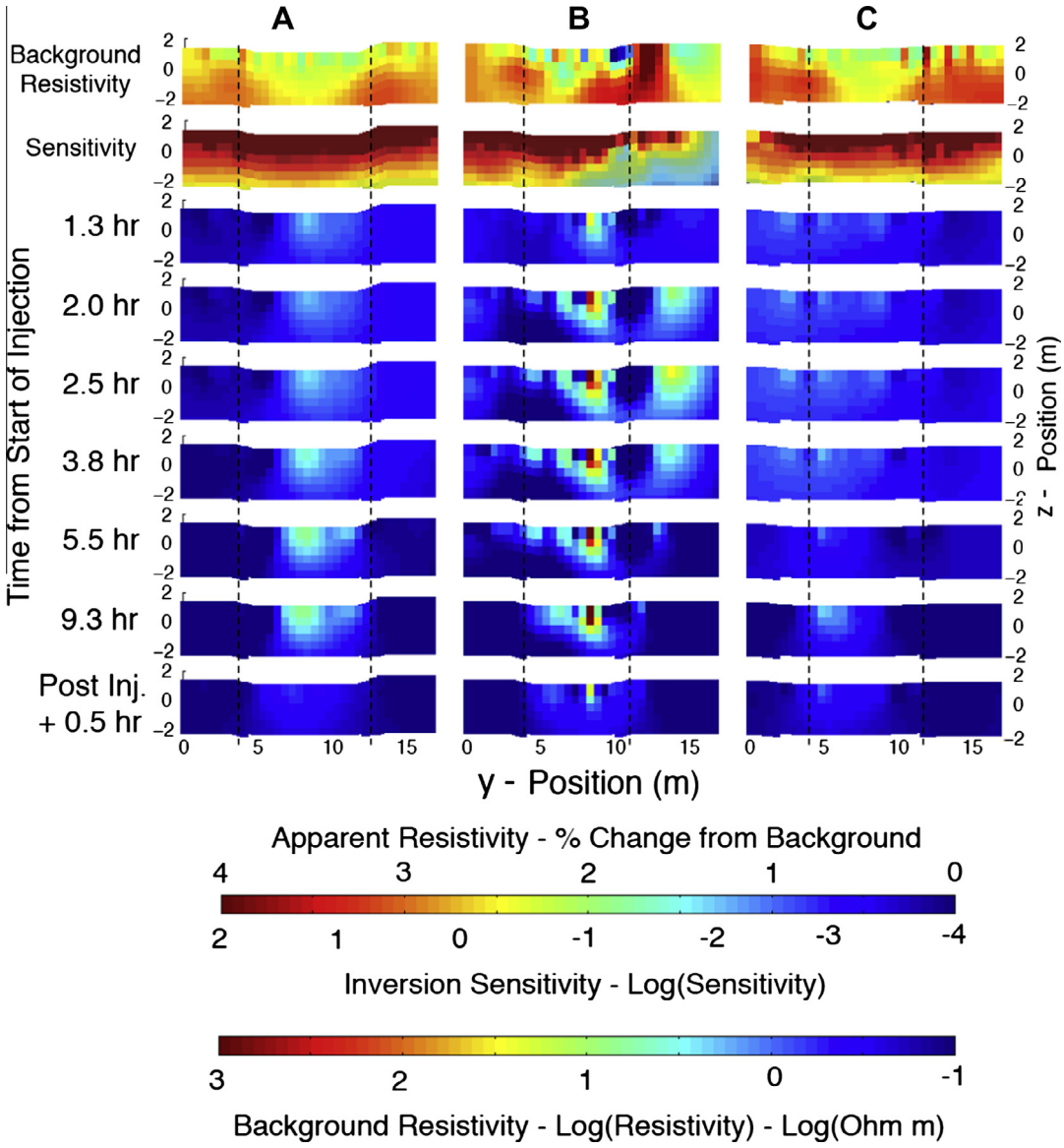

Fig. 5. Electrical resistivity imaging (ERI) tomograms from the three electrode transects: Left column – Transect 1 (T1); Middle column – Transect 2 (T2); and Right column – Transect 3. T1, T2, and T3 were located 20, 46, and 58 m, respectively, downstream of the injection zone. The artesian spring BR80 entered the stream ca. 30 m downstream of the injection zone. Top row – Pre-injection electrical resistivity background values. Transects are shown perpendicular to the stream with flow directed out of the page. The channel banks are identified by the dashed lines for each cross-section (R-bank on left; L-bank on right). *y* and *z* positions are assigned relative for each transect. 2nd row – Model sensitivity. 3rd – 8th row – Time-lapsed ERI results, at time elapsed after start of tracer addition. 9th row – Final ERI results collected after tracer addition ceased.

relative resistivity never substantially deviated from baseline values during the first 5.5 h of tracer addition. We propose the dark void was caused by water emerging from BR80 that overwhelmed or inhibited tracer penetration into this region, due to its proximity to T2. After 9.3 h of tracer addition, mixing between the tracer and BR80 appeared to decrease the influence of BR80 on hyporheic exchange occurring across T2. To the best of our knowledge, this represents the first time an artesian spring has been successfully imaged using ERI techniques.

ERI tomograms for T3 (Fig. 5C) were not as heterogeneous as those collected for T1 and revealed limited hyporheic exchange along this channel reach. Over the first 5.5 h of tracer addition the maximum $\Delta\rho$ for any single pixel never exceeded 2.1%. No physical pattern developed to resemble preferential infiltration of the tracer beneath the center of the channel. Interestingly, T3 was only 12 m downstream of T2 yet the complex distributions of varying subsurface resistivity observed at T2 had been homogenized by the time the tracer reached T3. This homogenization was not likely caused by greater dilution of the tracer between T2 and T3 because the relative decrease of in-stream conductivity was essentially the same at both of these locations (Fig. 3).

3.4. Flow path saturation

$\Delta\rho_{max}$ was defined as the greatest relative $\Delta\rho$ for a specified pixel area (Δy, Δz) at any given time as compared to the baseline resistivity. By analyzing the inversion data in terms of $\Delta\rho_{max}$, all time-lapse ERI images could be effectively collapsed into a single parameter that amplified the cross-section locations where the largest resistivity changes occurred (Fig. 6A). The highest and lowest $\Delta\rho_{max}$ values across T1 were 2.3% and 0.27%, respectively (Fig. 6A). The highest $\Delta\rho_{max}$ values occurred at the stream-bed surface along the center of the channel. High $\Delta\rho_{max}$ values also occurred in the subsurface, primarily beneath the center of the

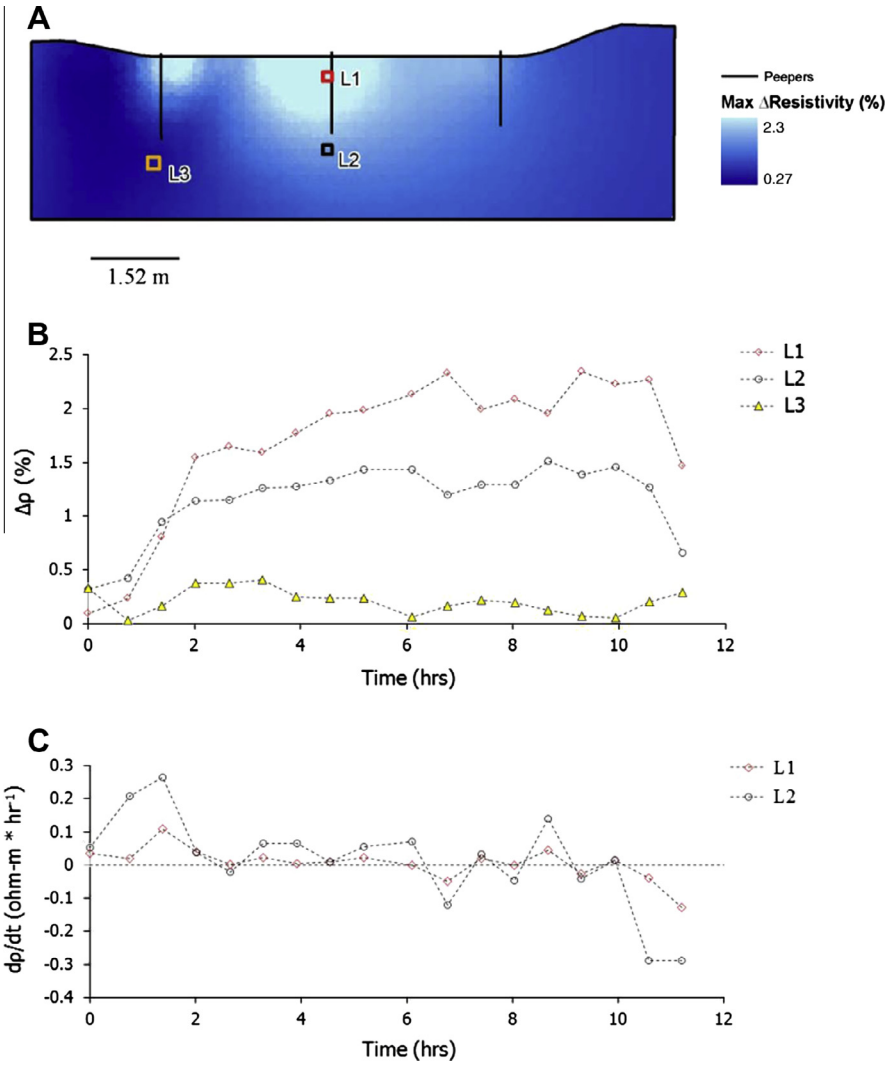

Fig. 6. (A) Maximum change in resistivity ($\Delta\rho_{max}$) resolved spatially at T1. The channel banks are identified by the indentation towards the top of the cross-section (R-bank on left; L-bank on right). (B) The corresponding temporal Δ resistivity at three finite element locations (L1, L2, and L3) shown in A. (C) Corresponding $d\rho/dt$ values as a function of time for finite elements L1 and L2.

channel, and represent substantial interactions between surface water and groundwater in the hyporheic zone. Because the tracer was injected for only 10 h, it was unknown whether, hypothetically, an infinite tracer addition time would result in a significant increase in the permeation radius of the tracer presented in Fig. 6A. Three pixel locations (L1, L2 and L3) in the 2-dimensional cross-section of T1 were compared over the duration of the test. Pixel locations were selected near the highest $\Delta\rho_{max}$ value (L1), an area of intermediate $\Delta\rho_{max}$ (L2), and an area presumably not influenced by the tracer (L3). At L1 and L2, comparable temporal trends were observed for the $\Delta\rho$ values (Fig. 6B). The $\Delta\rho$ values increased sharply in the first 2 h of tracer addition, stabilized to some extent over the next 8 h, and then decreased sharply after tracer addition ceased after 10 h. In contrast, L3 showed little to no change in $\Delta\rho$ versus time, confirming that the tracer had little to no influence at this location. The parameter $d\rho/dt$ was defined as the incremental relative $\Delta\rho$ for a specified pixel area between specified time intervals. Theoretically, as $d\rho/dt$ approaches zero, $\Delta\rho$ should approach a maximum value which indicates that the flow path through the pixel area has become saturated with the tracer. Saturated flow paths support the premise that the duration of tracer addition was adequate to visualize and quantify regions of preferential subsurface flow (e.g., hyporheic zones). Similar trends were observed for the parameter $d\rho/dt$ for locations L1 and L2 where $d\rho/dt$ was a positive value at the start of tracer addition, stabilized to near-zero values for the remainder of tracer addition, and then became negative after tracer addition ceased (Fig. 6C). The relatively higher magnitudes of $d\rho/dt$ at L2 suggest greater variability existed in this subsurface region as compared to L1. An interpretation of greater variability suggests the resistivity at L2 was approaching saturation slower relative to L1. Data from L3 were not presented in Fig. 6C; assuming no influence by the tracer.

Mean arrival time of the tracer was defined as the time when the $\Delta\rho$ for a pixel area first exceeded an arbitrary threshold value; indicating that the tracer had "arrived" at the specified location (Fig. 7A). Based on the range of $\Delta\rho_{max}$ values measured in the current study (0.27–2.3%), we used a threshold value ($\Delta\rho_{arrival}$) of 1.5%. This threshold value was chosen to confine the extent of radial change within the depth of trustworthy sensitivity. It was difficult, if not impossible, to assign quantitative values to these arrival times, as these 2-dimensional tomograms are generated by analyzing a 3-dimensional volume surrounding the transect. However, we propose that mean arrival times can serve as semi-quantitative proxies for relative groundwater velocities. In other

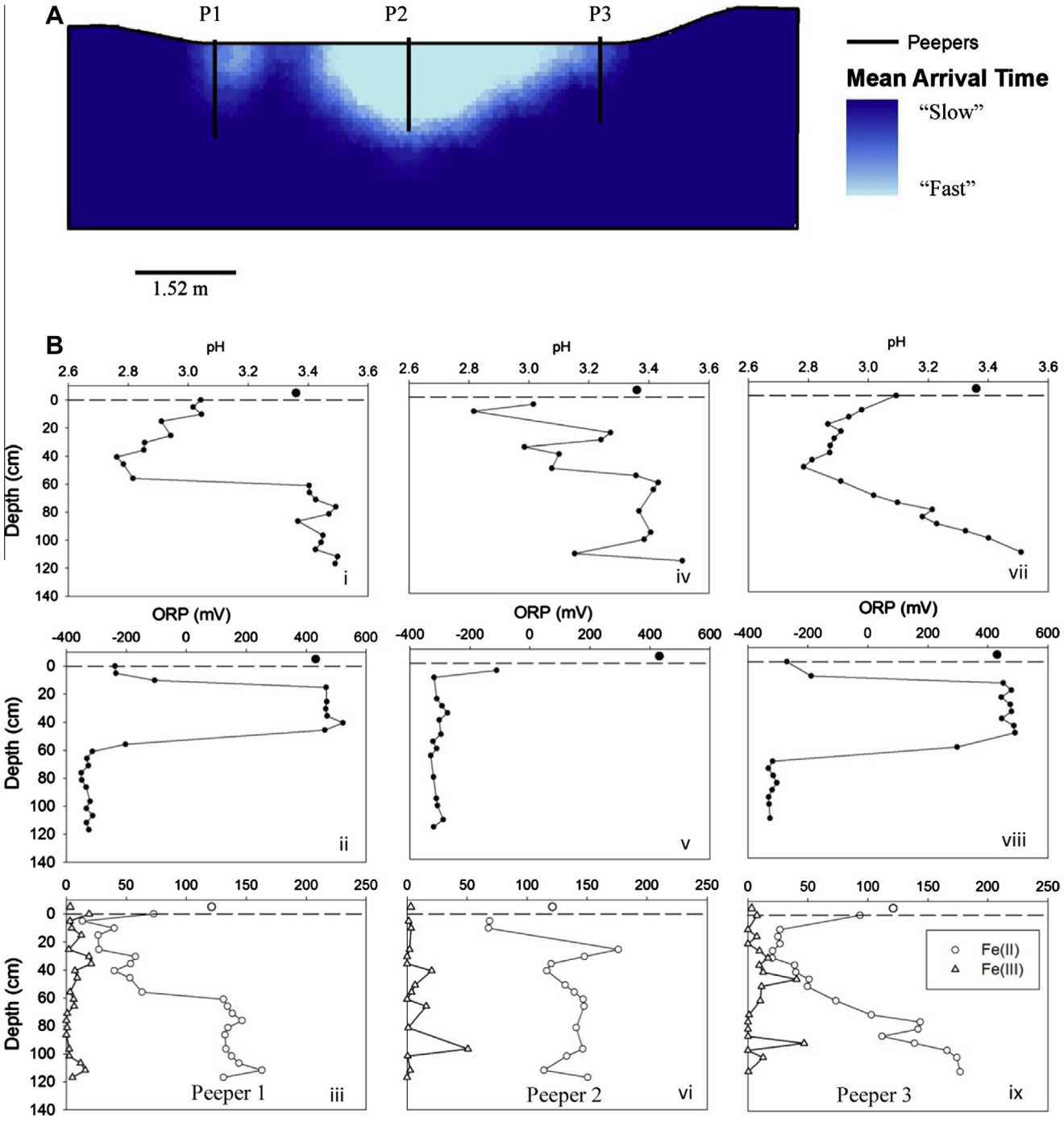

Fig. 7. (A) Relative mean arrival times resolved for transect 1 (T1). The channel banks are identified by the indentation towards the top of the cross-section (R-bank on left; L-bank on right). Black lines show the spatial locations of the subsurface porewater samplers (i.e., "peepers") to scale, and are labeled as P1, P2 and P3. (B) Geochemical results for pH (top row), oxidation–reduction potential (ORP) (middle row), and Fe speciation and concentration (mg/L) (bottom row) corresponding to P1, P2, and P3 (vertical columns). Surface water values are represented by larger symbols above the dashed line.

words, finite elements with shorter arrival times were located in regions of "fast" groundwater velocity while finite elements with longer arrival times were located in regions of "slow" groundwater velocity. Fast arrival times exceeded the threshold $\Delta\rho$ value during tracer addition. Slow arrival times exceeded the duration of tracer addition. Alternatively or additionally, pixels withshorter arrival times were located in regions of faster hyporheic exchange while finite elements with longer arrival times were located in regions of slower hyporheic exchange.

During this experiment, hyporheic exchange occurred predominantly as down-welling of the tracer and revealed hyporheic flow paths. During all other times, anoxic groundwater from the mine pool will likely up-well along these same hyporheic flow paths in this reach. Along T2, this up-welling manifests itself as the large artesian source at BR80. Along T1, this up-welling likely manifests itself along the radial distribution of flow paths visualized in Fig. 5A. The conceptual reversal of down-welling tracer (during ERI test) versus up-welling anoxic groundwater (during peeper

deployment months later) is important for interpreting subsurface geochemical depth profiles.

3.5. Subsurface pore-water chemistry

Vertical subsurface pore-water samplers were deployed across T1 for 28 d to investigate how subsurface geochemical profiles varied in regions of "fast" versus "slow" rates of hyporheic exchange (and groundwater velocity). The ERI methods identified that the most rapid exchange between surface and groundwater occurred near the center of the channel (Figs. 5 and 6A). The influence of the tracer was less substantial near the channel banks. Peepers 1 and 3 (P1 and P3) were installed in the streambed very close to the channel banks while peeper 2 (P2) was installed in the streambed directly in the center of the channel. Distinctly different geochemical depth profiles were found near the channel banks as compared to the channel center. At P1 the pH declined from 3.1 to <2.8 over the first 60 cm into the sediments, followed by a sharp increase in pH in between 60 and 65 cm, after which the pH stabilized between 3.4 and 3.5 from 65 cm to the final sample depth of 125 cm (Fig. 7B-ii). Also at P1, the ORP increased sharply from −220 mV nearest the surface to +450 mV at 15 cm into the sediments, stabilized at ca. +450 mV until 55 cm depth, decreased sharply to −350 mV at 60 cm depth, and then remained stable at ca. −350 mV from 65 cm to the final sample depth of 125 cm (Fig. 7B-iii). In-stream measurements for all parameters are presented as enlarged symbols just above 0 cm depth in all panels in Fig. 7B. At P1 the dissolved Fe(II) concentrations were below the in-stream concentration over the first 60 cm into the sediments; Fe(II) concentrations then increased sharply from 60 to 65 cm and stabilized at values above the in-stream concentration from 65 to 125 cm (Fig. 7B-iii). Similar subsurface geochemical trends were measured in P3 (Fig. 7-vii–ix); however, the increase in pH at depth was not a sharp gradient as compared to P1. While recognizing these differences, the more striking result was that the similar geochemical profiles at P1 and P3 could represent "symmetrical replicates" for the channel banks. Interpretations of these geochemical profiles are provided in Section 4.

Geochemical depth profiles beneath the center of the channel at P2 were distinctly different from the channel banks. At P2 the pH values changed inconsistently with depth but generally increased from ca. pH 2.9 to ca. pH 3.4 over the complete 125 cm profile (Fig. 7B-iv). No sharp pH gradient at any mid-depth location was observed (as seen at P1). At P2 the ORP decreased sharply from −100 mV at 5 cm into the sediments to −350 mV at 10 cm depth, and then remained stable at ca. −350 mV over the remainder of the profile (Fig. 7B-v). At P2 dissolved Fe(II) concentrations decreased to 65 mg/L at 5–10 cm into the sediments and then increased to 125–175 mg/L from 25 cm to the final sample depth of 125 cm (Fig. 7B-vi).

Collectively, these geochemical profiles demonstrated that subsurface zones of biological Fe(II) oxidation extended to greater depths beneath the channel banks as compared to the center of the channel. Biological Fe(II) oxidation will produce Fe(III) that will precipitate from solution (thus decreasing the dissolved Fe concentrations) and consume alkalinity (thus decreasing the pH). The presence of these sharp biogeochemical gradients, where sediments abruptly shift from Fe(II)-oxidizing to Fe(III)-reducing conditions, were also visually evident upon retrieval of the peepers. On P1 and P3, dark orange, Fe(III)-rich precipitates coated the peeper frames to an approximate depth of 60 cm. Below ca. 60 cm, the peeper frames were devoid of any mineral coatings. On P2 the Fe(III)-rich precipitates only coated the peeper frame to an approximate depth of 15 cm (photographs provided in Supplementary data). Low-pH biological Fe(III) reduction is expected to occur in these sediments based on previous studies (Senko et al., 2011). Many of the heterotrophic, acidophilic Fe(II)-oxidizing bacteria are also heterotrophic, acidophilic Fe(III)-reducers (Coupland and Johnson, 2008). Dissolved Fe(II) concentrations in the anoxic zones beneath the channel were typically higher than the in-stream Fe(II) concentrations, providing indirect geochemical evidence of Fe(III) reduction. While sulfide concentrations were not measured, no visual or olfactory evidence of sulfate reduction was observed in deep sediment samples.

4. Discussion

The physical conditions of Brubaker Run are important when trying to interpret subsurface geophysical and geochemical profiles. The large artesian spring uphill of the tracer injection zone provided the hydraulic head for both the surface water in the channel and the groundwater entering the channel. Prior to tracer addition, flow in the channel was 3.5 L/s at the top (0 m datum) and increased to 15.8 L/s at the bottom of the uni-directional channel (60 m downstream), due to contribution from BR80. The artesian spring at BR80 likely represents one large preferential flow path from the mine pool to the channel. ERI tomograms for T1 (Fig. 5A) demonstrate active hyporheic exchange in this reach (20 m downstream). Because the flow increases significantly from the top to the bottom of the channel, we presume that the channel near T1 is likely a gaining reach. Flow paths from the mine pool to this reach are likely more uniform, allowing the hyporheic zone to establish in a radial manner beneath the channel. The geochemistry of the groundwater that up-welled into the channel was essentially identical to the geochemistry of the uphill spring and the mine pool source. Because of the physical and hydrological complexities of this site, T1 provided an ideal setting to study the mixing of oxic surface water and anoxic groundwater and to measure subsurface geochemical profiles in areas of contrasting hyporheic exchange. Across T1, surface water hydrodynamics appeared to have a direct effect on the extent of hyporheic exchange beneath the channel. Surface water velocities were faster near the channel center (data not shown) while tracer penetration depths were greatest beneath the channel center (Fig. 5A). The extent of hyporheic exchange (Fig. 5A) and tracer arrival times (Fig. 7A) were lowest near the channel banks. Based on these 2-dimensional (Δy, Δz) representations of the system, flow paths from the groundwater to the channel banks are longer and slower as compared to flow paths to the channel center.

Subsurface pore-water chemistry (Fig. 7B) was directly influenced by the extent of hyporheic exchange (Fig. 5A) and rates of hyporheic exchange (Fig. 7A). Because of the greater mixing of anoxic groundwater with surface water, the subsurface pore-water beneath the channel center remained completely anoxic (Peeper 2; Fig. 7B-v). In contrast, a largevertical region (ca. 10–60 cm b.g.s.) of the subsurface pore-water beneath the channel banks was oxic (Peepers 1 and 3; Fig. 7B-ii and B-viii). One interpretation of these results is that because of less hyporheic exchange with the anoxic groundwater, $O_2(aq)$ in the surface water could penetrate to greater depths beneath the channel banks. However, measured values of low ORP in the near-surface sediments (0–10 cm b.g.s.) beneath the channel banks complicate this interpretation.

It is difficult to explain how $O_2(aq)$ can be delivered to intermediate depths of 10–60 cm b.g.s. and somehow bypass the overlying more reduced sediments. We are, however, confident in these measurements because they were observed in both Peepers 1 and 3 (symmetrical replicates of sorts). Based on visual observations of this site over several years, the accumulation of leaf litter and organic matter is not substantially variable between in-stream and on-land, nor between the stream bottom at the banks versus the center of the channel. Evidence of organic carbon cemented

into the sediments was found in all sediment cores collected from the site. We propose that the biological oxidation of this organic carbon, more so than dissolved Fe(II), created a highly reduced geochemical niche in the near-surface sediments. In other words, the rate of C oxidation exceeded the flux of $O_2(aq)$ into these sediments. A higher rate of C oxidation in these upper sediments may been due to the "fresher", more labile nature of this organic C as compared to organic C found deeper in the soil profile. We speculate that $O_2(aq)$ was then somehow delivered laterally into these deeper sediments (10–60 cm b.g.s.) from the dry land beyond the stream banks. Increased ORP values found deeper in the sediments represent a geochemical niche where the rate of Fe(II) oxidation did not exceed the flux of $O_2(aq)$. This geochemical niche is ideal for acidophilic, Fe(II)-oxidizing microbes. At even further depths (i.e., >80 cm b.g.s.), no $O_2(aq)$ penetrated into the sediments and little exchange of oxic surface water into the anoxic groundwater occurred. This deeper geochemical niche is ideal for acidophilic, Fe(III)-reducing microbes.

With respect to our applied objective of assessing the stability of Fe(III) sequestered in TIFs, it appears that (at least for this site) slow subsurface flow conditions may minimize the effect of Fe(III) reduction by minimizing the volume of its geochemical niche. Fe(III) reduction would lead to mineral dissolution and re-mobilization of Fe(II) and any associated trace metals or anions, compromising the effectiveness of TIFs for AMD treatment. Limiting the amount of organic matter that accumulates on and gets buried within the TIF should also help avoid the development of Fe(III)-reducing conditions. Provided that adequate land is available for an engineered TIF, slow flow conditions (both surface and subsurface) would also allow for greater Fe(II) oxidation and Fe removal.

With respect to our basic science objective, unique hydrogeochemical niches were identified in the subsurface beneath the AMD channel by overlaying tracer arrival times with pore-water chemistry profiles. Areas of relatively "fast" versus "slow" groundwater velocities were found beneath the center of the channel versus the channel banks, respectively (Fig. 7A). Areas of oxic versus anoxic conditions were found in shallow versus deep sediments, respectively, although the depth was strongly dependent on hyporheic exchange. When these data sets are combined, at least four unique hydrogeochemical niches can be identified: Fe(II)-oxidation in fast groundwater; Fe(II)-oxidation in slow groundwater; Fe(III)-reduction in fast groundwater, and; Fe(III)-reduction in slow groundwater.

Interstitial water velocities are known to influence redox processes in the hyporheic zone (Morrice et al., 2000). In a planimetric model of river meanders, the highest consumption of $O_2(aq)$ due to aerobic biogeochemical processes occurred in regions of relatively "slow" velocity or high sinuosity (Boano et al., 2010). In our system, where anoxic Fe(II)-rich water enters the hyporheic zone, regions of slow groundwater allowed for greater $O_2(aq)$ penetration. This in turn led to the highest consumption of Fe(II) (i.e., to greater depth) beneath the channel banks. It is still unknown how the different interstitial water velocities (i.e., fast versus slow) will affect the microbial communities in these subsurface environments.

In open channels, biofilm development and community structure are directly affected by hydrodynamic conditions. For example, in a study conducted on the development of microbial biofilms in microfluidic reactors, secondary flow features were shown to control biofilm architecture (Rusconi et al., 2011). In surface channels of AMD, Fe(II)-oxidizing bacteria capable of forming extracellular polymeric substances (EPS) have been observed to thrive in fast flowing waters (Hedrich and Johnson, 2012). Similarly, in subterranean streams in a sulfidic cave system, biofilm community structure appeared to be dependent on both primary (e.g., velocity) and secondary (e.g., eddy currents) hydrodynamic features (Macalady et al., 2008). It is likely that microbes that produce EPS and other hold-fast structures predominate in fast groundwater niches.

In the Fe(III)-reducing niches identified in our system, the mineral form of Fe(III) will likely exert an effect on Fe cycling and possibly on the microbial community structure. Several studies have shown that acidophilic Fe(II)-oxidizing bacteria are also capable of Fe(III)-reduction (Coupland and Johnson, 2008; Johnson et al., 2012; Lu et al., 2010). The potential for either process depends on geochemical conditions in the surrounding environment. Depending on the pH, schwertmannite precipitation will control Fe(III) solubility but will eventually transform to goethite (Schwertmann and Carlson, 2005). The kinetics of this transformation are relatively slow under low-pH conditions yet environmentally important over the time required for TIF maturation (months to years). Both minerals are used during dissimilatory Fe(III)-reduction, but Fe(III) in schwertmannite has been reported to be more bioavailable to heterotrophic iron(III)-reducing bacteria as compared to goethite (Lu et al., 2010). We would expect that sediments with a higher fraction of schwertmannite would support more Fe(III)-reducing activity. Future work will characterize the mineral assemblages and microbial communities found in these niches.

Acknowledgments

This research was supported by the Office of Surface Mining Reclamation and Enforcement under Cooperative Agreement (Grant) S11AC20005, and by the National Science Foundation Grant EAR-0911435. Any opinions, findings, and conclusions or recommendations expressed in this material are those of the author(s) and do not necessarily reflect the views of the National Science Foundation. Thanks to Dr. Scott Johnston, Southern Cross University, Australia, for loaning us the peepers used in this study.

Appendix A. Supplementary material

Supplementary data associated with this article can be found, in the online version, at http://dx.doi.org/10.1016/j.jhydrol.2013.08.007.

References

Baker, B.J., Banfield, J.F., 2003. Microbial communities in acid mine drainage. FEMS Microbiol. Ecol. 44 (2), 139–152.
Bigham, J.M., Schwertmann, U., Traina, S.J., Winland, R.L., Wolf, M., 1996. Schwertmannite and the chemical modeling of iron in acid sulfate waters. Geochim. Cosmochim. Acta 60 (12), 2111–2121.
Binley, A., Kemna, A., 2005. DC resistivity and induced polarization methods hydrogeophysics. In: Rubin, Y., Hubbard, S.S. (Eds.), Water Sci Technol. Library. Springer, Netherlands, pp. 129–156.
Boano, F., Demaria, A., Revelli, R., Ridolfi, L., 2010. Biogeochemical zonation due to intrameander hyporheic flow. Water Resour. Res. 46, W02511.
Bottacin-Busolin, A., Singer, G., Zaramella, M., Battin, T.J., Marion, A., 2009. Effects of streambed morphology and biofilm growth on the transient storage of solutes. Environ. Sci. Technol. 43 (19), 7337–7342.
Burgos, W.D. et al., 2012. Schwertmannite and Fe oxides formed by biological low-pH Fe(II) oxidation versus abiotic neutralization: impact on trace metal sequestration. Geochim. Cosmochim. Acta 76, 29–44.
Cardenas, M.B., Markowski, M.S., 2010. Geoelectrical imaging of hyporheic exchange and mixing of river water and groundwater in a large regulated river. Environ. Sci. Technol. 45 (4), 1407–1411.
Coscia, I., Greenhalgh, S.A., Linde, N., Doetsch, J., Marescot, L., Günther, T., Vogt, T., Green, A.G., 2011. 3D crosshole ERT for aquifer characterization and monitoring of infiltrating river water. Geophys. 76 (2), G49–G59.
Coupland, K., Johnson, D.B., 2008. Evidence that the potential for dissimilatory ferric iron reduction is widespread among acidophilic heterotrophic bacteria. FEMS Microbiol. Lett. 279 (1), 30–35.
Cravotta, C.A., 2008. Dissolved metals and associated constituents in abandoned coal-mine discharges, Pennsylvania, USA. Part 1: Constituent quantities and correlations. Appl. Geochem. 23 (2), 166–202.
DeSa, T., Brown, J., Burgos, W., 2010. Laboratory and field-scale evaluation of low-pH Fe(II) oxidation at Hughes Borehole, Portage, Pennsylvania. Mine Water Environ. 29 (4), 239–247.

Doro, K.O., Leven, C., Cirpka, O.A., 2013. Delineating subsurface heterogeneity at a loop of River Steinlach using geophysical and hydrogeological methods. Environ. Earth Sci., 1–14.
Ebraheem, A.M., Hamburger, M.W., Bayless, E.R., Krothe, N.C., 1990. A study of acid mine drainage using earth resistivity measurements. Ground Water 28 (3), 361–368.
Flores, G.E. et al., 2012. Inter-field variability in the microbial communities of hydrothermal vent deposits from a back-arc basin. Geobiol. 10 (4), 333–346.
Gooseff, M.N., 2010. Defining hyporheic zones – advancing our conceptual and operational definitions of where stream water and groundwater meet. Geogr. Compass 4, 945–955.
Hedrich, S., Johnson, D.B., 2012. A modular continuous flow reactor system for the selective bio-oxidation of iron and precipitation of schwertmannite from mine-impacted waters. Bioresour. Technol. 106, 44–49.
Hesslein, R.H., 1976. *In situ* sampler for close interval pore water studies. Limnol. Oceanogr. 21 (6), 912–914.
Johnson, D.B., Kanao, T., Hedrich, S., 2012. Redox transformations of iron at extremely low pH: fundamental and applied aspects. Front. Microbiol. 3.
Johnston, S.G. et al., 2009. Pore water sampling in acid sulfate soils: a new peeper method. J. Environ. Qual. 38 (6), 2474–2477.
Kirby, C.S., Cravotta, C.A., 2005. Net alkalinity and net acidity 1: theoretical considerations. Appl. Geochem. 20 (10), 1920–1940.
Lu, S., Gischkat, S., Reiche, M., Akob, D.M., Hallberg, K.B., Kusel, K., 2010. Ecophysiology of fe-cycling bacteria in acidic sediments. Appl. Environ. Microbiol. 76, 8174–8183.
Macalady, J.L. et al., 2008. Niche differentiation among sulfur-oxidizing bacterial populations in cave waters. ISME J. 2 (6), 590–601.
Merkel, R.H., 1972. The use of resistivity techniques to delineate acid mine drainage in ground water. Ground Water 10 (5), 38–42.
Morrice, J.A., Dahm, C.N., Valett, H.M., Unnikrishna, P.V., Campana, M.E., 2000. Terminal electron accepting processes in the alluvial sediments of a headwater stream. J. N. Am. Benthol. Soc. 19, 593–608.
Nyquist, J.E., Freyer, P.A., Toran, L., 2008. Stream bottom resistivity tomography to map ground water discharge. Ground Water 46 (4), 561–569.
Rucker, D.F., Glaser, D.R., Osborne, T., Maehl, W.C., 2009. Electrical resistivity characterization of a reclaimed gold mine to delineate acid rock drainage pathways. Mine Water Environ. 28 (2), 146–157.
Rusconi, R., Lecuyer, S., Autrusson, N., Guglielmini, L., Stone, H.A., 2011. Secondary flow as a mechanism for the formation of biofilm streamers. Biophys. J. 100, 1392–1399.
Sánchez España, J., Santofimia Pastor, E., López Pamo, E., 2007. Iron terraces in acid mine drainage systems: a discussion about the organic and inorganic factors involved in their formation through observations from the Tintillo acidic river (Riotinto mine, Huelva, Spain). Geosphys. 3 (3), 133–151.
Schwertmann, U., Carlson, L., 2005. The pH-dependent transformation of schwertmannite to goethite at 25 °C. Clay Miner. 40, 63–66.
Senko, J., Bertel, D., Quick, T., Burgos, W., 2011. The influence of phototrophic biomass on Fe and S redox cycling in an acid mine drainage-impacted system. Mine Water Environ. 30 (1), 38–46.
Stookey, L.L., 1970. Ferrozine – a new spectrophotometric reagent for iron. Anal. Chem. 42 (7), 779–781.
Toran, L., Hughes, B., Nyquist, J., Ryan, R., 2012. Using hydrogeophysics to monitor change in hyporheic flow around stream restoration structures. Environ. Eng. Geosci. 18 (1), 83–97.
Veysey Ii, J., Goldenfeld, N., 2008. Watching rocks grow. Nat. Phys. 4 (4), 310–313.
Ward, A.S., Gooseff, M.N., Singha, K., 2010. Imaging hyporheic zone solute transport using electrical resistivity. Hydrol. Process. 24 (7), 948–953.